

Research Article

Artificial Neural Networks Based Friction Law for Elastomeric Materials Applied in Finite Element Sliding Contact Simulations

Aleksandra Serafińska, Wolfgang Graf, and Michael Kaliske 

Institute for Structural Analysis, Technische Universität Dresden, D-01062 Dresden, Germany

Correspondence should be addressed to Michael Kaliske; michael.kaliske@tu-dresden.de

Received 5 July 2018; Accepted 2 October 2018; Published 19 November 2018

Academic Editor: Francisco J. Montáns

Copyright © 2018 Aleksandra Serafińska et al. This is an open access article distributed under the Creative Commons Attribution License, which permits unrestricted use, distribution, and reproduction in any medium, provided the original work is properly cited.

A realistic characterization of the frictional behaviour of materials and mechanical systems is of prime importance for the assessment of their contact interaction properties, especially in the context of undesired temperature rise or intensive wear leading to service life reduction. A characteristic tribological property of elastomeric materials is the dependency of the friction coefficient on the local contact pressure, sliding velocity, and temperature in the contact interface. Thus, the friction coefficient is not constant in the entire contact area but varies according to the magnitudes of the aforementioned three influencing factors. In this contribution, a friction law based on artificial neural networks (ANN) is presented, which is able to capture the nonlinear dependencies of the friction coefficient on the contact pressure, sliding velocity, and temperature. Due to an extraordinary adaptivity of the ANN structure, these nonlinear relations stemming from experimental data can be modelled properly within the introduced friction law, in contrast to other friction formulations, which are limited by the fitting quality of their parameters. The ANN based friction law is implemented into a contact formulation of the finite element method (FEM). Especially, the linearization of contact contributions to the weak form of momentum balance equation, required for the FEM, is developed taking into account the differentiability of the ANN. The applicability of the developed friction law within the finite element analysis of tires as well as within sliding simulations of rubber elements is presented in this paper.

1. Introduction

In this contribution, a novel method enabling to capture the thermo-mechanical frictional characteristics of materials and mechanical systems is developed. An accurate modelling of frictional properties is crucial for the assessment of structural durability, since the friction energy dissipation in the contact interface can lead to pronounced wear [1] and temperature increase. Thereby, the intensification of both these effects results commonly in a material failure or degradation of surfaces in contact.

In order to model the friction phenomena of elastomeric structures in its whole complexity, the dependency of the friction coefficient on the contact pressure, sliding velocity, and temperature as well as on the topology of contacting surfaces has to be captured.

When considering the friction of elastomeric structures with respect to surface roughness, two contributions

determining the magnitude of the friction coefficient can be distinguished, the hysteresis and adhesion contribution [2]. Hysteresis friction is related to an internal energy dissipation appearing in viscoelastic materials during sliding over rough surfaces. On the other hand, adhesion friction results from intermolecular, distance-dependent interaction forces between two surfaces, which are pronounced especially on flat surfaces.

Analytical approaches introducing friction theories considering surface roughness are proposed by Klüppel and Heinrich [2, 3] as well as by Persson [4]. Furthermore, numerical approaches for the modelling of friction are developed, which are based on the finite element method, multiscale analysis, and homogenization; see [5–7].

For the analysis of the frictional behaviour of mechanical systems, which are commonly performed at a structural level, macroscopic friction laws are predominantly applied. These formulations do not consider surface roughness and

frictional properties at multiple scales. They rather provide formulations for the dependency of tangential stresses or the friction coefficient on the local contact pressure, sliding velocity, and temperature in the contact interface. These dependencies are developed for certain materials in contact. Such macroscopic friction laws are proposed in [8–10].

The friction law introduced in this contribution also belongs to the category of macroscopic friction laws. Though, while other macroscopic equations for friction commonly take into account only one or two mentioned factors, which influence the magnitude of the friction coefficient, the herein presented method enables to account for all three factors and can be even extended to more aspects, if required.

In the proposed constitutive equation for friction, meta-models in form of response surfaces based on artificial neural networks [11] are implemented within the friction formulation. Due to an outstanding adaptivity of the ANNs, the fitting quality to the experimental results is commonly higher than the one obtained for other friction formulations. Furthermore, the differentiability of the ANN formulation enables a direct specification of linearization terms of contact contributions to the weak form of momentum balance equation, required for the Newton method to find the solution. Thus, a straightforward implementation into the FEM is feasible.

A further advantage of the introduced friction law is its temperature dependency, which enables the application of the law within thermo-mechanically coupled FE analyses. This fact is of significant importance, since the properties of elastomeric materials change distinctively due to the influence of temperature.

The benefits of the utilization of ANNs in various engineering tasks and disciplines have been noticed in many publications; e.g., in [12], an overview of the application of ANNs in civil engineering is presented. ANNs have been introduced to material law formulations; see [13–15]. Furthermore, ANNs are commonly employed for the approximation of a response surface, which can substitute the computational model of the structural analysis, compare [16, 17]. Moreover, the application of ANNs to structural analysis with uncertain data [18] and to pattern recognition approaches (see [19]) is known from the literature, though, an ANN based friction law characterized by a consistent formulation for the FEM, applicable to thermo-mechanically coupled analysis, is still an unexplored topic and, thus, in the scope of this contribution.

This paper is structured as follows. In Section 2, the results of an experimental investigation of friction properties are presented and a friction coefficient response surface approximation on the basis of ANN is shown. In Section 3, the architecture and the training procedure of the applied feed-forward artificial neural network are introduced. Section 4 is devoted to the formulation of the proposed metamodel based friction law and its implementation into the framework of the FEM. Finally, in Section 5 three examples visualizing the results of the FE analysis of elastomeric structures under the application of the developed friction formulation are presented.

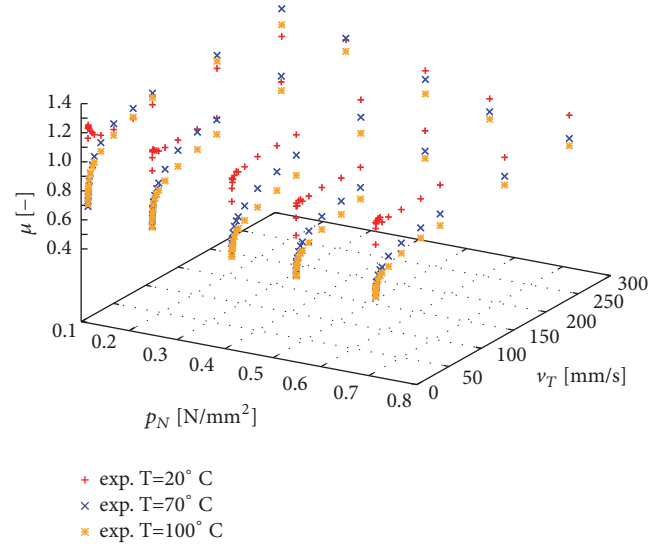


FIGURE 1: Friction coefficient at various contact pressures p_N , sliding velocities v_T , and temperatures T .

2. Friction Coefficient Response Surface Based on Experimental Data

The constitutive equation for friction investigated in this contribution is formulated as

$$\mathbf{t}_T = \mu(|p_N|, \|\mathbf{v}_T\|, T) |p_N| \frac{\mathbf{g}_T}{\|\mathbf{g}_T\|}, \quad (1)$$

where \mathbf{t}_T denotes the tangential stress, \mathbf{g}_T stands for the tangential slip, and μ is the friction coefficient. Thereby, the dependency of the friction coefficient on the normal pressure p_N , the sliding velocity v_T , and the temperature T is considered.

In order to identify the frictional properties of rubber and to account for the aforementioned friction coefficient formulation, experimental investigations including friction tests on a tribometer are conducted. Rubber samples of size 20x20x4 mm stemming from the tire tread pattern are subjected to frictional contact with a granite surface. Within the test, various temperature, velocity, and normal load (pressure) conditions are applied to identify the dependency of the friction coefficient on these factors. Especially, the temperature range $T = [20, 100]^\circ\text{C}$, the normal pressure range $p_N = [0.114, 0.714] \text{ N/mm}^2$, and the velocity range $v_T = [0.1, 300] \text{ mm/s}$ are tested. In each single experiment, the rubber block is subjected to a prescribed normal pressure, sliding velocity and temperature. Thereby, in every experiment nearly constant temperature conditions are provided since the rubber samples are preheated to a predefined temperature and the experiment is executed in a climate chamber with the same predefined indoor temperature. The tested rubber sample is fixed to a cantilever arm, which transmits the normal load and is subjected to contact with a disc rotating at a prescribed velocity.

In Figure 1, the results of the friction test are visualized. Thereby, a decrease of the friction coefficient with increasing

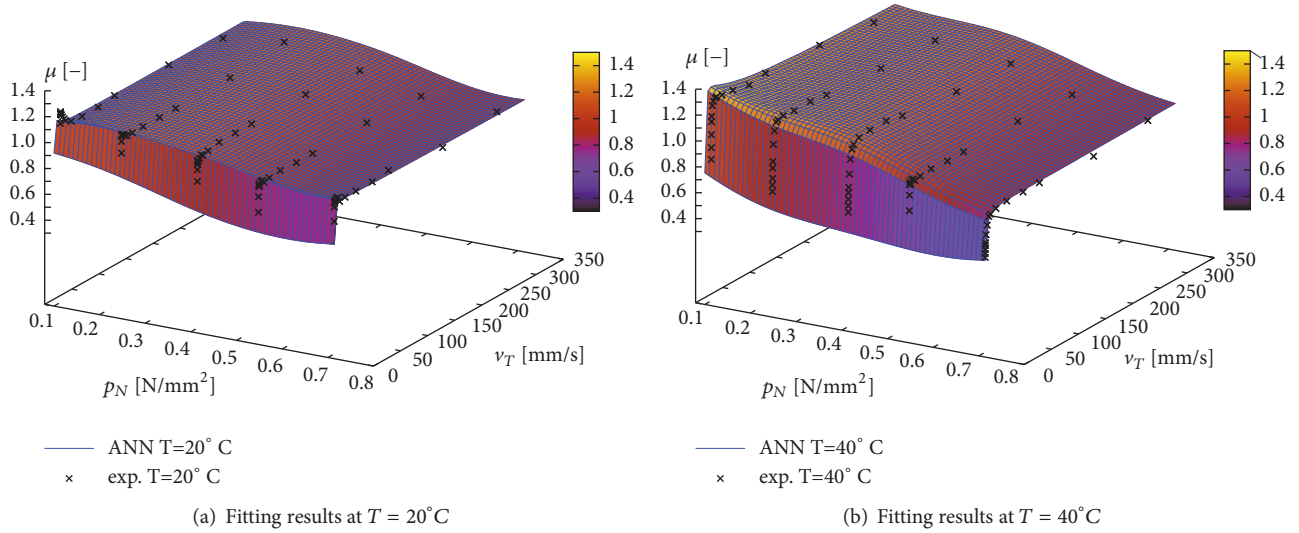


FIGURE 2: Friction coefficient response surfaces provided by ANN for experimental results at $T = 20^\circ\text{C}$ and $T = 40^\circ\text{C}$.

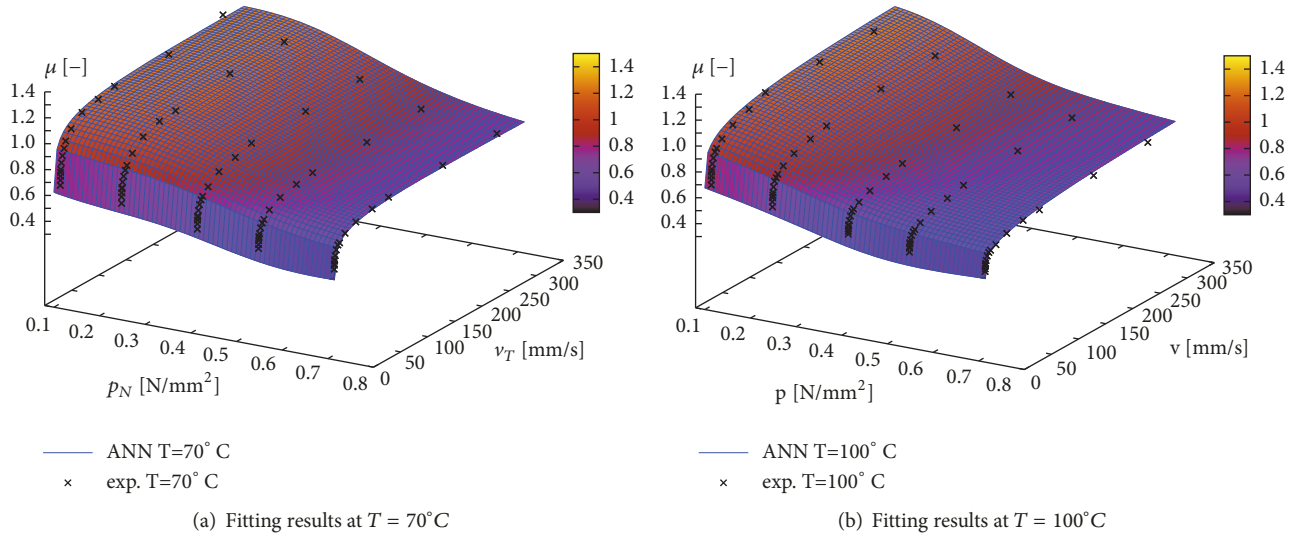


FIGURE 3: Friction coefficient response surfaces provided by ANN for experimental results at $T = 70^\circ\text{C}$ and $T = 100^\circ\text{C}$.

rubber temperature can be observed, except in the low pressure and high sliding velocity regimes. Furthermore, a steep ascent of the friction coefficient in the low sliding velocity range and a moderate ascending friction coefficient values in higher sliding velocity ranges are shown in Figure 1. Finally, the relation of the friction coefficient to the normal pressure is defined by decreasing μ magnitudes with the increasing p_N magnitudes.

In this contribution, a metamodel in form of an artificial neural network is developed, which is able to reproduce all the mentioned dependencies $\mu(p_N, v_T, T)$ with a very high accuracy. Furthermore, a single ANN is able to provide friction coefficient response surfaces at various temperatures, compare Figure 1. An advantage of such a response surface is the availability of the friction coefficient values interpolated between the measured friction coefficient magnitudes.

In Figures 2 and 3, the response surfaces provided by an ANN at tread block temperatures $T = 20, 40, 70, 100^\circ\text{C}$ are visualized. Due to its extraordinary adaptivity, a single ANN is able to reproduce various shapes of response surfaces at subsequent temperature levels.

Especially, the friction coefficient response surfaces at $T = 20^\circ\text{C}$ and $T = 40^\circ\text{C}$ are characterized by a steep ascent of the friction coefficient in low sliding velocity range and a flattening of the surface in higher sliding velocity range. On the other hand, the response surfaces at $T = 70^\circ\text{C}$ and $T = 100^\circ\text{C}$ show a smooth transition between the region with a steep ascent of the friction coefficient and the flatter region.

In order to visualize the high fitting quality of the ANN, cut-offs from response surfaces presented in Figures 2 and 3 at certain normal pressures $p_N = 0.248 \text{ N/mm}^2$ and $p_N = 0.548 \text{ N/mm}^2$ are prepared; see Figure 4. The friction

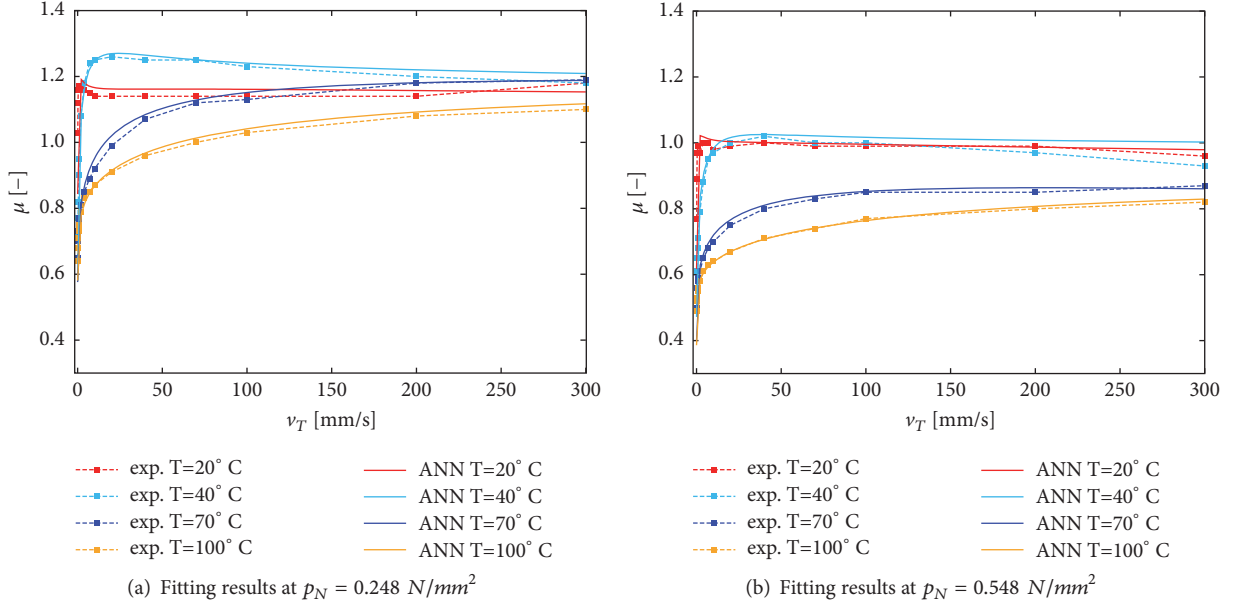


FIGURE 4: Friction coefficient μ provided by ANN versus experimental result at normal pressure $p_N = 0.248 \text{ N/mm}^2$ and $p_N = 0.548 \text{ N/mm}^2$ and at various temperatures.

coefficients computed by the ANN match the experimental results with a very high accuracy. All dependencies including the decrease of the friction coefficient with the increase of temperature and with the increase of normal pressure are captured by the developed metamodel.

As a reference solution for the developed metamodel based friction law, the Huemer friction law [8] enhanced by the temperature dependency is applied. The Huemer friction law is formulated as

$$\mathbf{t}_T = \mu_H |p_N| \frac{\Delta \mathbf{g}_T}{\|\Delta \mathbf{g}_T\|}, \quad (2)$$

where the friction coefficient μ_H is represented by

$$\mu_H = \frac{\alpha |p_N|^{n-1} + \beta}{a + b/\|\mathbf{v}_T\|^{1/m} + c/\|\mathbf{v}_T\|^{2/m}}. \quad (3)$$

The free parameters of the Huemer friction law $\alpha, \beta, a, b, c, m, n$ are fitted for the experimental data available at four temperature levels $T = 20, 40, 70, 100^\circ\text{C}$ corresponding to constant rubber block temperatures; see Figure 1. Taking into account the obtained four parameter sets, each parameter can be considered as temperature dependent $\alpha(T), \beta(T), a(T), b(T), c(T), m(T), n(T)$. In this way, the formulation of the Huemer friction law is extended by the temperature dependency.

In Figure 5, the friction coefficients obtained by the Huemer friction law are plotted versus the experimental results at normal pressures $p_N = 0.248 \text{ N/mm}^2$ and $p_N = 0.548 \text{ N/mm}^2$. Although for each temperature level, a separate set of parameters, which best approximates the experimental results, has been used, the fitting quality of the extended Huemer friction law is not as good as of the

metamodel based friction law. Especially, in the high sliding velocity regime, the friction coefficients computed within the Huemer friction law differ from the experimentally identified friction coefficients. Thereby, it should be noticed that a single metamodel is able to generate friction coefficient response surfaces at various temperature levels, whereas for the Huemer friction law, a separate parameter set is required to reproduce the friction coefficients at a certain temperature.

3. Architecture of Artificial Neural Networks

In this section, the architecture of the feedforward artificial neural network applied to the approximation of the friction coefficient response surfaces, presented in Section 2, is described. Since the structure of an ANN mimics the one of the human brain, two main structural components, neurons and synapses, can be distinguished, compare [11]. Thereby, the functionality of neurons as the information processing units involves a mapping of the neuron input signal x_i onto the output signal θ_j ; see Figure 6. Synapses, constituting the connections between two neurons i and j , are able to transmit the signal, which can be additionally strengthened or weakened according to the respective weight ω_{ij} of the synaptical connection.

Within a neuron j , the aggregation of the input signals x_i , which are multiplied by the synaptical weights ω_{ij} , is accomplished by the summing junction functionality

$$u_j = \sum_{i=1}^n \omega_{ij} x_i + v_j. \quad (4)$$

In (4), v_j stands for a bias term. Subsequently, the summing junction u_j is evaluated by an activation function \mathcal{F} yielding the neuron output signal θ_j ; see Figure 6. Within the

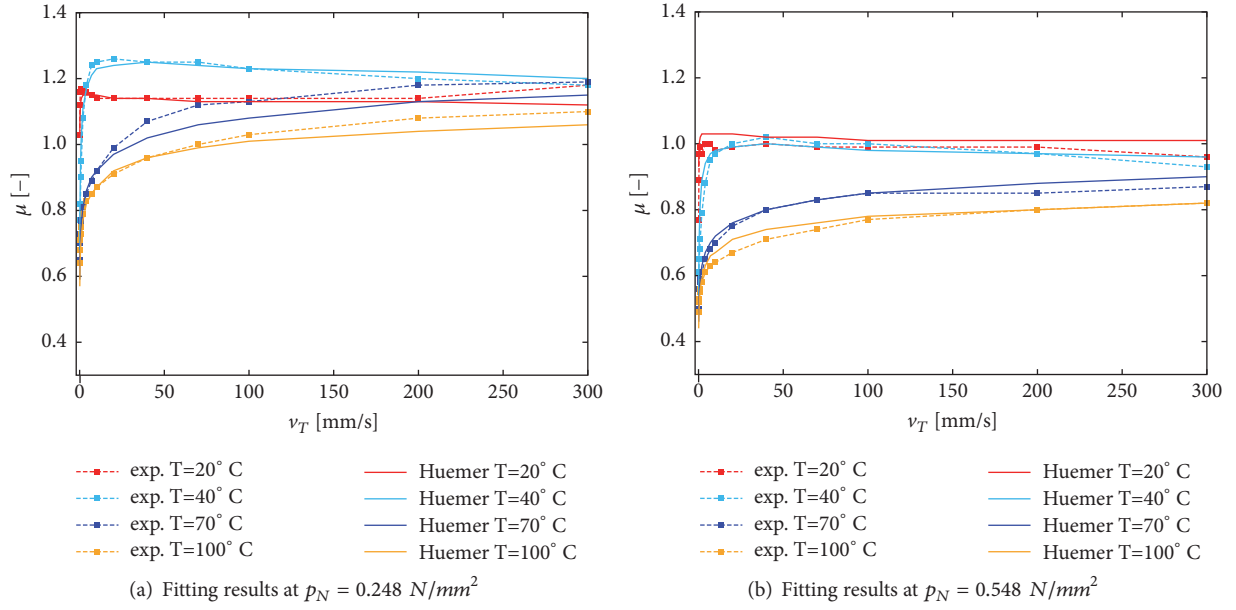


FIGURE 5: Friction coefficient μ provided by the Huemer friction law versus experimental result at normal pressure $p_N = 0.248 \text{ N/mm}^2$ and $p_N = 0.548 \text{ N/mm}^2$ and at various temperatures.

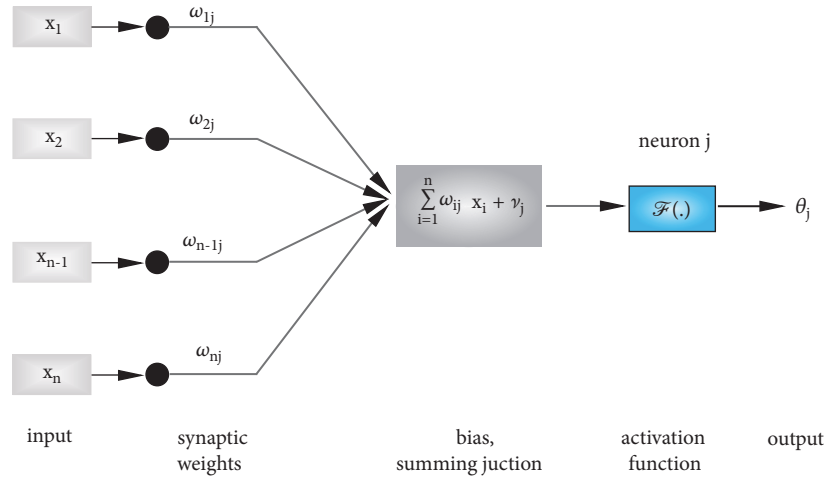


FIGURE 6: Information processing within a neuron.

developed ANN, logistic sigmoid functions are implemented as activation functions due to their advantageous properties, e.g., nonlinearity and differentiability

$$\theta_j = \mathcal{F}(u_j) = \frac{1}{1 + e^{-\sum_{i=1}^n \omega_{ij} x_i + v_j}}. \quad (5)$$

Within the artificial neural network architecture, neurons belong to one of three layer types, the input, the hidden and the output layer. For the approximation of the friction coefficient response surface an ANN with an input layer containing three neurons, which process the normal pressure p_N , the velocity v_T , and the temperature T as the input signals, is applied; see Figure 7. The selected ANN contains one hidden layer with 14 neurons and an output layer with a single

neuron returning the computed friction coefficient μ_{ann} as the output signal θ_k .

Since in this approach the feedforward neural networks are utilized, one-directional information flow is assumed. The output signal of each neuron is transmitted to several neurons of the following layer by synaptical connections.

3.1. Training Procedure. The ANN with the presented structure is provided by a procedure for the identification of an optimal ANN architecture. The optimization algorithm analyses various configurations of hidden layers, especially their number as well as the number of neurons within each layer, and identifies an architecture providing best fitting to

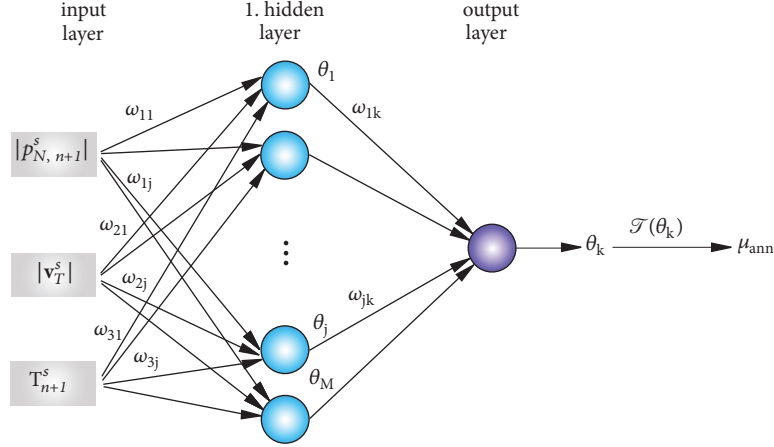


FIGURE 7: Architecture of an ANN applied for the computation of the friction coefficient μ_{ann} .

the experimental results. The ANN input signals x_i , $i = 1, 2, 3$, which enter the training procedure, are normalized

$$|x_i^s| = S(|x_i|) = \frac{|x_i| - \mu_{x_i}}{\sigma_{x_i}}. \quad (6)$$

Thereby, $x_i \in [p_N, v_T, T]$ are the contact pressures, sliding velocities and temperatures evaluated within the friction test. The function S accounts for the Gaussian distribution of experimental x_i magnitudes, where μ_{x_i} stands for the mean value and σ_{x_i} for the standard deviation.

The training of the feedforward ANN is executed by means of a backpropagation algorithm [11]. This method computes the gradient of an error function, which is defined as a difference between the experimental friction coefficient and the one provided by ANN, to identify the optimal configuration of synaptical weights ω_{ij} .

3.2. Computation of the Friction Coefficient by the ANN. A fitted ANN is applied within a friction law and enables the computation of the friction coefficient, which succeeds in several steps. First, the outcome of the hidden layer neuron θ_j is calculated for the normalized ANN input quantities $p_{N, n+1}^s$, v_T^s and T_{n+1}^s , which stem from the FE analysis

$$\begin{aligned} \theta_j &= \mathcal{F} \left(\sum_{i=1}^3 \omega_{ij} x_i + \nu_j \right) \\ &= \mathcal{F} \left(\omega_{1j} |p_{N, n+1}^s| + \omega_{2j} \|v_T^s\| + \omega_{3j} T_{n+1}^s + \nu_j \right). \end{aligned} \quad (7)$$

Thereby, ω_{ij} stands for the synaptical weight associated with a neural connection between the input layer neuron i and the hidden layer neuron j , whereas ν_j defines a bias term of the hidden layer neuron. Second, the outcome of the output layer neuron θ_k is calculated

$$\theta_k = \mathcal{F} \left(\sum_{j=1}^M \omega_{jk} \theta_j + \nu_k \right), \quad (8)$$

where ω_{jk} is the synaptical weight of the neural connection between the hidden layer neuron j and the output layer neuron k and ν_k is the bias term of the output layer neuron accordingly.

Finally, the output layer signal θ_k is evaluated by the transformation function \mathcal{F} to provide the friction coefficient μ_{ann}

$$\mu_{ann} = \mathcal{F}(\theta_k) = k_{sc} \operatorname{arctanh}(2\theta_k - 1). \quad (9)$$

Thereby, k_{sc} is the scale factor of the friction coefficient, which is calculated during the training procedure. The transformation function \mathcal{F} aims to scale the normalized signals processed within the ANN back to the real output parameter range.

The friction coefficient μ_{ann} computed by the ANN is evaluated within the friction law presented in (1), which is applied in the finite element simulation framework

$$\mathbf{t}_T = \mu_{ann}(|p_N|, \|v_T\|, T) |p_N| \frac{\mathbf{g}_T}{\|\mathbf{g}_T\|}. \quad (10)$$

4. Temperature-Dependent Friction Law Based on ANN

4.1. Friction in the Contact Formulation of the FEM. In the FEM, formulations for the tangential contact and friction are employed when two bodies slide on each other. Thereby, a stick and slip state as well as a transition zone between these states is considered in the tangential contact; see Figure 8. Especially, the slip state occurs if, due to the acting tangential force F_H , the critical tangential stress is achieved. In order to enable a smooth transition between the stick and slip state and to avoid differentiability problems in this zone, the hyperbolic tangent regularization is applied; see Figure 8. Thus, (10) results in

$$\mathbf{t}_T = \mu_{ann}(|p_N|, \|v_T\|, T) |p_N| \tanh \left(\frac{\|\Delta \mathbf{g}_T\|}{\beta} \right) \frac{\Delta \mathbf{g}_T}{\|\Delta \mathbf{g}_T\|}. \quad (11)$$

The hyperbolic tangent regularization, marked by a dashed line in Figure 8, is specified in dependency on the tangential

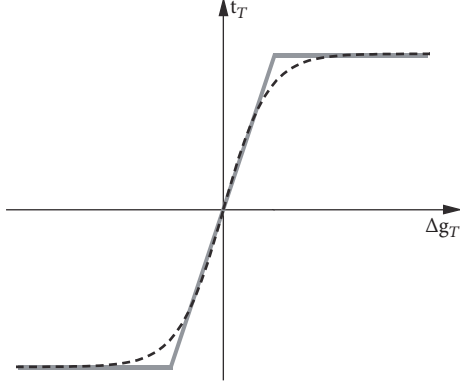


FIGURE 8: Regularization of the stick-slip relation.

slip rate $\Delta \mathbf{g}_T$ and the regularization coefficient β ; see [20]. Especially, while only minor relative slips are regarded during the sticking state, the magnitude of relative motion increases with the increase of the tangential stress \mathbf{t}_T until the critical \mathbf{t}_T and the slip state is reached. How close the regularized stick-slip transition approximates the classical double-branch transition depends on the magnitude of the coefficient β .

If in the FE analysis contact between two bodies is established at some position, the associated contact constraint is set active and the following penalty term is added to the expression for the total energy

$$\Pi_c = \frac{1}{2} \int_{\Gamma_c} (\epsilon_N (g_N)^2 + \mathbf{t}_T \cdot \mathbf{g}_T) dA, \quad \epsilon_N > 0. \quad (12)$$

Thereby, g_N denotes the penetration function within the normal contact formulation and Γ_c is the surface boundary in contact. In (12), $\epsilon_N = 10 \cdot k_{rep}$ stands for the penalty term and k_{rep} is the representative underlying element stiffness.

The minimization of the total energy, which leads to the weak form of the balance of momentum, requires the variation of (12)

$$\delta \Pi_c = \int_{\Gamma_c} (\epsilon_N g_N \delta g_N + \mathbf{t}_T \cdot \delta \mathbf{g}_T) dA, \quad \epsilon_N > 0. \quad (13)$$

Finally, the linearization of the weak form of balance of momentum needs to be provided for the Newton method to find the solution of the system of equations and, thus, a formulation for the linearized contact contribution is specified

$$d\delta \Pi_c = \int_{\Gamma_c} (dg_N \epsilon_N \delta g_N + d\delta g_N \epsilon_N g_N + d\mathbf{t}_T \cdot \delta \mathbf{g}_T + d\delta \mathbf{g}_T \cdot \mathbf{t}_T) dA. \quad (14)$$

Equation (14) contains a term defining the linearized tangential stress $d\mathbf{t}_T$, which is computed considering the developed constitutive equation for friction. Especially, since in (11) the tangential stresses are specified in dependency on the contact pressure, sliding velocity and temperature, the expression $d\mathbf{t}_T$

is a function of the derivatives of tangential stresses \mathbf{t}_T with respect to p_N , \mathbf{g}_T , and T

$$d\mathbf{t}_T = \frac{\partial \mathbf{t}_T}{\partial p_N} dp_N + \frac{\partial \mathbf{t}_T}{\partial \mathbf{g}_T} d\mathbf{g}_T + \frac{\partial \mathbf{t}_T}{\partial T} dT. \quad (15)$$

The formulation of these derivatives is given in the following section.

4.2. Linearization Terms for the Implementation of the Friction Law within the FEM. The implementation of the developed ANN based friction law within the framework of the FE analysis requires the specification of the algorithmic tangent including the derivatives of the tangential stresses $\partial \mathbf{t}_T / \partial p_N$, $\partial \mathbf{t}_T / \partial \mathbf{g}_T$, and $\partial \mathbf{t}_T / \partial T$.

The tangential stresses and their derivatives are computed in each time step t_{n+1} of the FE analysis based on the developed friction law. Thus, (11) results in

$$\mathbf{t}_{T,n+1} = \mu_{ann}(|p_{N,n+1}|, \|\mathbf{v}_T\|, T_{n+1}) \tanh\left(\frac{\|\Delta \mathbf{g}_T\|}{\beta}\right) \cdot |p_{N,n+1}| \frac{\Delta \mathbf{g}_T}{\|\Delta \mathbf{g}_T\|}. \quad (16)$$

For a simplified formulation of the derivatives of tangential stresses $\mathbf{t}_{T,n+1}$, the following notation of (16) is introduced:

$$\mathbf{t}_{T,n+1} = C_{fr,n+1} \mathbf{n}_{n+1}, \quad (17)$$

with $\mathbf{n}_{n+1} = \Delta \mathbf{g}_T / \|\Delta \mathbf{g}_T\|$ and C_{fr} defined as

$$C_{fr,n+1} = \mu_{ann}(|p_{N,n+1}|, \|\mathbf{v}_T\|, T_{n+1}) \tanh\left(\frac{\|\Delta \mathbf{g}_T\|}{\beta}\right) \cdot |p_{N,n+1}|. \quad (18)$$

First, the derivative of the tangential stress $\mathbf{t}_{T,n+1}$ with respect to the contact pressure $p_{N,n+1}$ is specified as

$$\frac{\partial \mathbf{t}_{T,n+1}}{\partial p_{N,n+1}} = \frac{\partial C_{fr,n+1}}{\partial |p_{N,n+1}|} \frac{\partial |p_{N,n+1}|}{\partial p_{N,n+1}} \mathbf{n}_{n+1}, \quad (19)$$

with

$$\frac{\partial C_{fr,n+1}}{\partial |p_{N,n+1}|} = \frac{\partial \mu_{ann}}{\partial |p_{N,n+1}|} \tanh\left(\frac{\|\Delta \mathbf{g}_T\|}{\beta}\right) |p_{N,n+1}| + \mu_{ann} \tanh\left(\frac{\|\Delta \mathbf{g}_T\|}{\beta}\right), \quad (20)$$

$$\frac{\partial |p_{N,n+1}|}{\partial p_{N,n+1}} = \text{sign}(p_{N,n+1}) = -1 \quad \text{for } p_{N,n+1} < 0. \quad (21)$$

Please note that, in (20), the derivative $\partial \mu_{ann} / \partial |p_{N,n+1}|$ is computed taking into account the architecture and the properties of the underlying ANN, which is presented later in this section.

Second, the derivative of tangential stress $\mathbf{t}_{T,n+1}$ with respect to the tangential slip $\mathbf{g}_{T,n+1}$ is formulated as

$$\frac{\partial \mathbf{t}_{T,n+1}}{\partial \mathbf{g}_{T,n+1}} = \mathbf{n}_{n+1} \otimes \frac{\partial C_{fr,n+1}}{\partial \mathbf{g}_{T,n+1}} + C_{fr,n+1} \frac{\partial \mathbf{n}_{T,n+1}}{\partial \mathbf{g}_{T,n+1}}, \quad (22)$$

where

$$\begin{aligned} \frac{\partial C_{fr,n+1}}{\partial \mathbf{g}_{T,n+1}} &= \frac{\partial \mu_{ann}}{\partial \mathbf{g}_{T,n+1}} \tanh\left(\frac{\|\Delta \mathbf{g}_T\|}{\beta}\right) |p_{N,n+1}| \\ &+ \frac{\partial (\tanh(\|\Delta \mathbf{g}_T\|/\beta))}{\partial \mathbf{g}_{T,n+1}} \mu_{ann} |p_{N,n+1}|. \end{aligned} \quad (23)$$

The formulation of the derivative of the friction coefficient μ_{ann} with respect to the tangential slip $\mathbf{g}_{T,n+1}$ in (23) is based on the formulation of the sliding velocity \mathbf{v}_T

$$\frac{\partial \mu_{ann}}{\partial \mathbf{g}_{T,n+1}} = \frac{\partial \mu_{ann}}{\partial \|\mathbf{v}_T\|} \frac{\partial \|\mathbf{v}_T\|}{\partial \mathbf{g}_{T,n+1}}. \quad (24)$$

Thereby, the derivative $\partial \mu_{ann} / \partial \|\mathbf{v}_T\|$ is computed considering the differentiability and the architecture of the ANN.

Taking into account the dependency between the sliding velocity $\|\mathbf{v}_T\|$ and the tangential slip $\mathbf{g}_{T,n+1}$, $\|\mathbf{v}_T\| = \|\Delta \mathbf{g}_T\| / \Delta t$, where $\Delta \mathbf{g}_T = \mathbf{g}_{T,n+1} - \mathbf{g}_{T,n}$, yields

$$\frac{\partial \|\mathbf{v}_T\|}{\partial \mathbf{g}_{T,n+1}} = \frac{\partial \|\mathbf{v}_T\|}{\partial \Delta \mathbf{g}_T} \cdot \frac{\partial \Delta \mathbf{g}_T}{\partial \mathbf{g}_{T,n+1}} = \frac{1}{\Delta t} \frac{\Delta \mathbf{g}_T}{\|\Delta \mathbf{g}_T\|} \cdot \mathbf{I}, \quad (25)$$

where \mathbf{I} is the second order identity tensor.

To complete the formulation in (23), the derivative of the hyperbolic tangent regularization term is specified

$$\begin{aligned} &\frac{\partial (\tanh(\|\Delta \mathbf{g}_T\|/\beta))}{\partial \mathbf{g}_{T,n+1}} \\ &= \left(1 - \tanh^2\left(\frac{\|\Delta \mathbf{g}_T\|}{\beta}\right)\right) \frac{1}{\beta} \frac{\Delta \mathbf{g}_T}{\|\Delta \mathbf{g}_T\|} \cdot \mathbf{I}. \end{aligned} \quad (26)$$

The last term required for the specification of the derivative $\partial \mathbf{t}_{T,n+1} / \partial \mathbf{g}_{T,n+1}$ in (22) is given by

$$\frac{\partial \mathbf{n}_{n+1}}{\partial \mathbf{g}_{T,n+1}} = \frac{\partial \mathbf{n}_{n+1}}{\partial \Delta \mathbf{g}_T} \cdot \frac{\partial \Delta \mathbf{g}_T}{\partial \mathbf{g}_{T,n+1}} = \frac{\partial \mathbf{n}_{n+1}}{\partial \Delta \mathbf{g}_T} \cdot \mathbf{I}, \quad (27)$$

where

$$\frac{\partial \mathbf{n}_{n+1}}{\partial \Delta \mathbf{g}_T} = \frac{1}{\|\Delta \mathbf{g}_T\|} (\mathbf{I} - \mathbf{n}_{n+1} \otimes \mathbf{n}_{n+1}). \quad (28)$$

Finally, the expression for the derivative of the tangential stress $\mathbf{t}_{T,n+1}$ with respect to the temperature T_{n+1} is given, as a last part of the formulation of the algorithmic tangent

$$\frac{\partial \mathbf{t}_{T,n+1}}{\partial T_{n+1}} = \frac{\partial C_{fr,n+1}}{\partial T_{n+1}} \mathbf{n}_{n+1}, \quad (29)$$

where

$$\frac{\partial C_{fr,n+1}}{\partial T_{n+1}} = \frac{\partial \mu_{ann}}{\partial T_{n+1}} \tanh\left(\frac{\|\Delta \mathbf{g}_T\|}{\beta}\right) |p_{N,n+1}|. \quad (30)$$

The introduced equations specifying the algorithmic tangent require the computation of the derivatives $\partial \mu_{ann} / \partial |p_{N,n+1}|$, $\partial \mu_{ann} / \partial \|\mathbf{v}_T\|$, and $\partial \mu_{ann} / \partial T_{n+1}$, which refer to the formulation of the friction coefficient computed by the ANN. Especially, the calculation of these derivatives is conditioned by the differentiability of the ANN formulation as well as of the applied activation function. In this work, sigmoid logistic activation functions are utilized, for which the derivative equals to

$$\mathcal{F}' = \mathcal{F} (1 - \mathcal{F}). \quad (31)$$

From the formulation of the friction coefficient given in (9) and from the definition of the neuronal output shown in (7) and (8), the derivative $\partial \mu_{ann} / \partial |p_{N,n+1}|$ is specified as

$$\frac{\partial \mu_{ann}}{\partial |p_{N,n+1}|} = \frac{\partial \mu_{ann}}{\partial \theta_k} \frac{\partial \theta_k}{\partial |p_{N,n+1}^s|} \frac{\partial |p_{N,n+1}^s|}{\partial |p_{N,n+1}|}, \quad (32)$$

with

$$\begin{aligned} \frac{\partial \theta_k}{\partial |p_{N,n+1}^s|} &= \frac{\partial \theta_k}{\partial \theta_j} \frac{\partial \theta_j}{\partial |p_{N,n+1}^s|} = \mathcal{F}' \left(\sum_{j=1}^M w_{jk} \theta_j + \nu_k \right) \\ &\cdot \mathcal{F}' (w_{1j} |p_{N,n+1}^s| + w_{2j} \|\mathbf{v}_T^s\| + w_{3j} T_{n+1}^s + \nu_j). \end{aligned} \quad (33)$$

Considering (31), the expression in (33) can be rewritten as

$$\frac{\partial \theta_k}{\partial |p_{N,n+1}^s|} = \theta_k (1 - \theta_k) \sum_{j=1}^M w_{jk} \theta_j (1 - \theta_j) w_{1j}. \quad (34)$$

In a similar way, the derivative $\partial \mu_{ann} / \partial \|\mathbf{v}_T\|$ is formulated

$$\frac{\partial \mu_{ann}}{\partial \|\mathbf{v}_T\|} = \frac{\partial \mu_{ann}}{\partial \theta_k} \frac{\partial \theta_k}{\partial \|\mathbf{v}_T^s\|} \frac{\partial \|\mathbf{v}_T^s\|}{\partial \|\mathbf{v}_T\|}, \quad (35)$$

where

$$\frac{\partial \theta_k}{\partial \|\mathbf{v}_T^s\|} = \theta_k (1 - \theta_k) \sum_{j=1}^M w_{jk} \theta_j (1 - \theta_j) w_{2j}. \quad (36)$$

The derivative $\partial \mu_{ann} / \partial T_{n+1}$ is specified analogously to the derivatives $\partial \mu_{ann} / \partial |p_{N,n+1}|$ and $\partial \mu_{ann} / \partial \|\mathbf{v}_T\|$

$$\frac{\partial \mu_{ann}}{\partial T_{n+1}} = \frac{\partial \mu_{ann}}{\partial \theta_k} \frac{\partial \theta_k}{\partial T_{n+1}^s} \frac{\partial T_{n+1}^s}{\partial T_{n+1}}, \quad (37)$$

where

$$\frac{\partial \theta_k}{\partial T_{n+1}^s} = \theta_k (1 - \theta_k) \sum_{j=1}^M w_{jk} \theta_j (1 - \theta_j) w_{3j}. \quad (38)$$

For the formulation of the derivatives in (32), (35), and (37), terms accounting for the transformation function \mathcal{T} and the normalization function S are defined as

$$\frac{\partial \mu_{am}}{\partial \theta_k} = \frac{\partial \mathcal{T}(\theta_k)}{\partial \theta_k} = \frac{-1}{2(\theta_k^2 - \theta_k)}, \quad (39)$$

$$\frac{\partial |p_{N,n+1}^s|}{\partial |p_{N,n+1}|} = \frac{\partial S(|p_{N,n+1}|)}{\partial |p_{N,n+1}|} = \frac{1}{\sigma_{p_N}}, \quad (40)$$

$$\frac{\partial \|\mathbf{v}_T^s\|}{\partial \|\mathbf{v}_T\|} = \frac{\partial S(\|\mathbf{v}_T\|)}{\partial \|\mathbf{v}_T\|} = \frac{1}{\sigma_{v_T}},$$

$$\frac{\partial T_{n+1}^s}{\partial T_{n+1}} = \frac{\partial S(T_{n+1})}{\partial T_{n+1}} = \frac{1}{\sigma_T}. \quad (41)$$

5. FE Frictional Contact Simulation of Elastomeric Structures

The developed metamodel based friction formulation is applied for the investigation of contact properties of elastomeric structures and elements. Three examples are prepared. First, an isothermal FE simulation of a rubber block sliding on a rigid surface is carried out, whereas various rubber block temperatures are applied to assess their influence on the tangential stresses in the contact interface. Second, a fully thermo-mechanically coupled FE analysis of a rubber block with tread pattern moving on a tire-rotation-like displacement path is accomplished to quantify the performance of the friction law in a thermo-mechanically coupled simulation. Finally, isothermal FE analyses of a tire in a steady state rolling situation are carried out to visualize the applicability of the friction law within the steady state transport analysis, which is based on the arbitrary Lagrangian-Eulerian approach.

In all three examples, the constitutive behaviour of rubber is described by a hyperelastic material formulation utilizing the Marlow model; see [21]. The strain energy density is determined in the Marlow model by

$$W(I_1) = \int_0^{\lambda_T(I_1)-1} T(\epsilon) d\epsilon, \quad (42)$$

where I_1 is the first invariant of the left Cauchy-Green strain tensor $\mathbf{B} = \mathbf{F}\mathbf{F}^T$ and \mathbf{F} is the deformation gradient. In (42), ϵ denotes the uniaxial strain, $T(\epsilon)$ the nominal uniaxial traction, and $\lambda_T(I_1)$ stands for the uniaxial stretch obtained as a solution of the following equation

$$\lambda_T(I_1)^3 - I_1 \lambda_T(I_1) + 2 = 0. \quad (43)$$

In order to define $T(\epsilon)$, a uniaxial test data set is applied. The Marlow model is selected for the implementation within the following examples due to its straightforward formulation by means of only the first invariant I_1 . Several hyperelastic material models, as the Yeoh model [22] or the Arruda & Boyce model [23], are specified using only the first invariant I_1 as well, though they are characterized by a certain mathematical formulation with various parameters, which need to be fitted. Contrarily, in the Marlow model the material

TABLE 1: Loading and boundary conditions in the simulation of a sliding rubber block.

$p_N = 0.248 \text{ MPa}$		$p_N = 0.548 \text{ MPa}$	
$\mathbf{v}_T = 70 \text{ mm/s}$		$\mathbf{v}_T = 70 \text{ mm/s}$	
Sim	$T[^\circ\text{C}]$	Sim	$T[^\circ\text{C}]$
1	20	4	20
2	70	5	70
3	100	6	100

response is determined solely by the test data in form of uniaxial stress-strain curve, which integration yields directly the strain energy density, as shown in equation (42). The idea of modelling rubber as a viscoelastic material, which is presented, e.g., in the model by Simo [24], Reese & Govindjee [25], or Holzapfel [26], is not followed in this contribution but could be introduced within the following examples without any restrictions.

In all examples, the artificial neural network presented in Sections 2 and 3 with an architecture comprised of 3 input layer neurons, 14 hidden layer neurons, and 1 output layer neuron is applied.

5.1. Rubber Block Sliding on a Rigid Surface. Within the first example, a rubber block sliding on a fixed rigid surface is investigated. The rubber block is subjected to a normal pressure p_N applied uniformly at the top of the block and moves with a constant velocity \mathbf{v}_T ; see Figure 9. The rubber block has a prescribed initial temperature T , which remains constant during the simulation due to the isothermal conditions within the simulation.

In this example, two normal pressure magnitudes $p_N = 0.248 \text{ MPa}$ and $p_N = 0.548 \text{ MPa}$ are investigated; see Table 1, whereas for each p_N three rubber block temperatures $T = [20, 70, 100]^\circ\text{C}$ are prescribed. Thereby, in all six simulations, a sliding velocity $\mathbf{v}_T = 70 \text{ mm/s}$ is applied.

The rubber block is discretized by 8-node solid elements. The application of the newly developed friction law accounting for the dependency of μ on the nodal p_N , \mathbf{v}_T , and T magnitudes enables an adequate computation of the tangential stresses.

In Figure 9, the tangential stresses \mathbf{t}_T obtained in all six simulations are plotted against the tangential slip \mathbf{g}_T . Thereby, in each graph, the sticking regime with minor elastic slip magnitudes, the transition zone between sticking and sliding and the sliding regime with a constant \mathbf{t}_T magnitude are clearly visible. Furthermore, a significant influence of the temperature-dependent formulation of the friction law on the course of tangential stresses is apparent from Figure 9. Especially, at $p_N = 0.248 \text{ MPa}$ as well as at $p_N = 0.548 \text{ MPa}$, \mathbf{t}_T decreases with increasing temperature T , which is conform with experimental results presented in Figure 1. This simple example shows that sticking, sliding, and the transition between these states can be simulated properly with the developed formulation of the friction law.

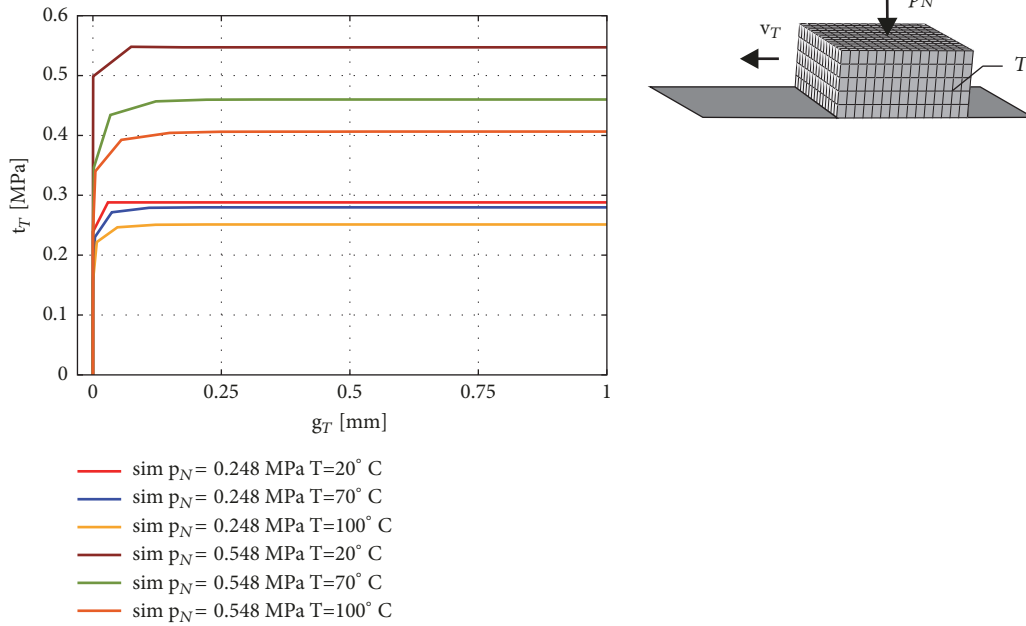


FIGURE 9: Tangential stresses in the rubber block simulation in dependency on temperature and normal pressure.

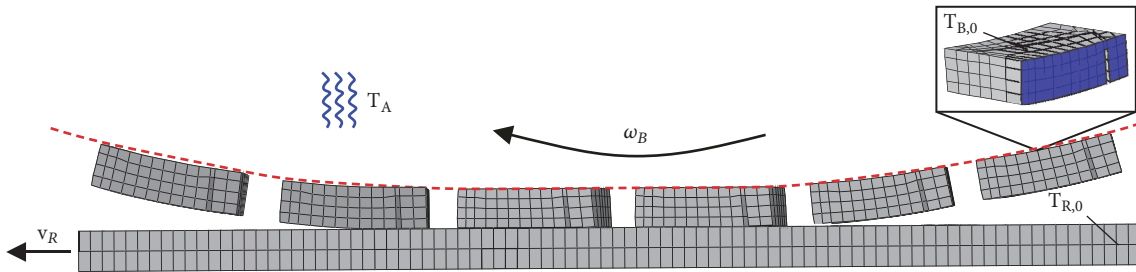


FIGURE 10: Rubber block moving on a tire-rotation-like displacement path.

5.2. Rubber Block Moving on a Tire-Rotation-Like Displacement Path. In the second example, the proposed friction formulation is applied to a thermo-mechanically coupled FE analysis of a rubber block moving on a tire-rotation-like displacement path. In Figure 10, the considered rubber block with tread pattern is visualized. Furthermore, the movement of the block along a displacement path is presented, which consists of three steps including the establishment of contact between the rubber block and the road, the sliding of the block at the road surface, and the final step, where the block detaches from the road surface.

A tire in a standard operating condition is subjected to angular and translational velocity, whereas the magnitudes of these velocities determine whether braking, acceleration or a free rolling state is obtained. Analogously, these states can be achieved in the presented simulation of the rubber block by applying a translation velocity v_R to the road and letting the block move on a displacement path according to a prescribed angular velocity ω_B ; see Figure 10.

In the applied thermo-mechanically coupled simulation, two heat sources can be identified. First, the temperature

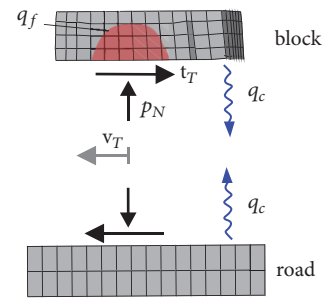


FIGURE 11: Rubber block-road contact interface.

increase in the contact interface due to friction energy dissipation is considered. Second, the heat exchange between the rubber block and surrounding air influences the rubber block temperature; see Figure 11. The prescribed initial temperatures of the rubber block and the road are denoted by $T_{B,0}$ and $T_{R,0}$, respectively, whereas the air temperature is denoted by T_A ; compare Figure 10.

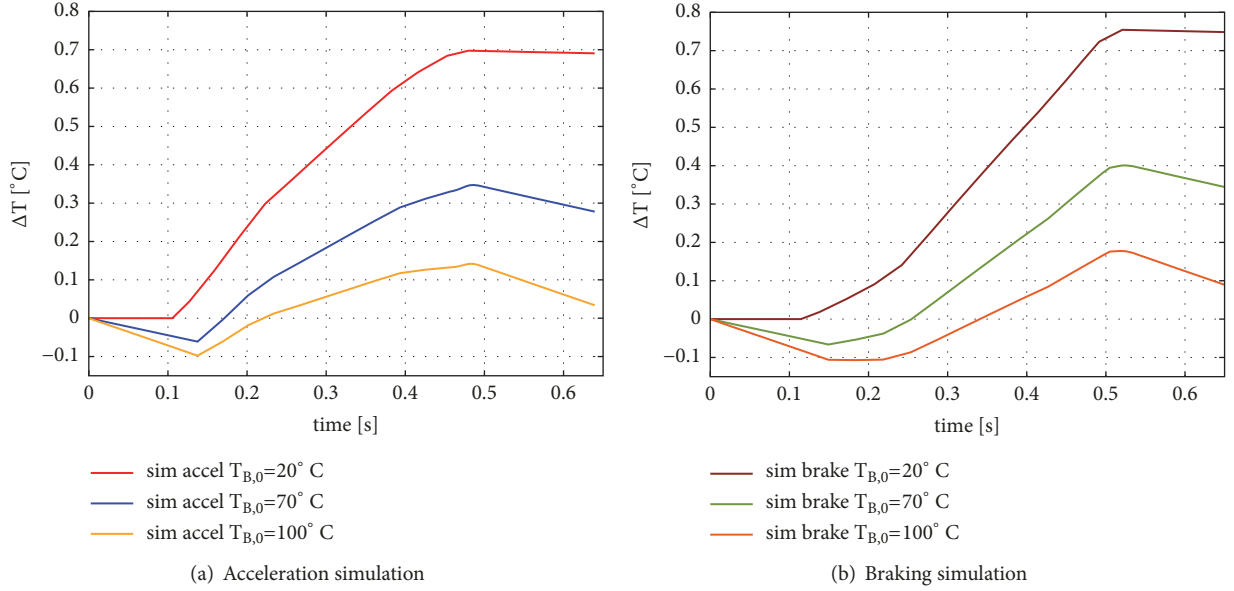


FIGURE 12: Temperature amplitude in the acceleration and braking simulation.

The heat flux q_f arising due to the friction energy dissipation in the contact interface is defined as

$$q_f = \eta f \mathcal{D}_s, \quad (44)$$

where \mathcal{D}_s is the friction energy, η is the fraction of \mathcal{D}_s converted into heat, and f is the heat distribution factor between the two surfaces in contact. While η and f take values from the interval $[0, 1]$, the friction energy \mathcal{D}_s is given as

$$\mathcal{D}_s = \mathbf{t}_T \dot{\mathbf{g}}_T. \quad (45)$$

The heat flux q_c arising due to the heat exchange between the rubber block and the surrounding air is defined as

$$q_c = h(T_B - T_A), \quad (46)$$

where h stands for the film coefficient. The left and right side as well as the bottom of the block, marked by blue shaded surface in Figure 10, are subjected to the heat exchange with the surrounding air. The remaining surfaces of the block are assumed to be in contact with other tire parts.

Both, the rubber block and the road, are modelled as flexible bodies, which are discretized by 8-node solid elements with displacements and temperature degrees of freedom. The road is modelled as a linear elastic material with temperature-dependent Young's modulus. The applied magnitudes of the thermal conductivity k , the specific heat c_p and the Young's modulus E are given in Table 2.

In this example, two types of simulation are performed, the first one capturing the accelerating and the second one the braking condition. These conditions are defined by the relation of the angular and the translational velocity, compare Table 3. Furthermore, for each simulation type, three initial rubber block temperatures $T_{B,0} = [20, 70, 100]^\circ\text{C}$ are considered. The initial road temperature is set to $T_{R,0} =$

TABLE 2: Material properties in the simulation of a rubber block moving on a tire-rotation-like displacement path.

	rubber material	road material
k [W/mK]	0.279	0.9
c_p [J/kgK]	$2010 \cdot 10^6$	$1200 \cdot 10^6$
E [MPa]	-	2200 at $T_R = 20^\circ\text{C}$
		1300 at $T_R = 100^\circ\text{C}$
		530 at $T_R = 200^\circ\text{C}$

20°C and the air temperature to $T_A = 20^\circ\text{C}$ in all simulations. Further quantities required for the computation of heat fluxes are defined as $\eta = 1$, $h = 22 \cdot 10^{-1} \text{W/mm}^2\text{K}$, $f = 0.8$, whereas f denotes the heat distribution factor determining the heat flux into the block surface.

In Figures 12 and 13, the results of the accelerating and braking simulation are plotted for a chosen node in the bottom surface of the rubber block, which is contacting the road. In Figure 12, the temperature amplitude $\Delta T = T_{B,i} - T_{B,0}$, defined as a difference between the nodal temperature $T_{B,i}$ in the i th time increment and the initial temperature $T_{B,0}$ is plotted over the simulation time. Thereby, in Figure 12(a) the results of the accelerating simulation and in Figure 12(b) the results of the braking simulation performed at various initial rubber block temperatures $T_{B,0}$ are visualized.

Within Figure 12(a), the three stages of the simulation can be clearly identified, first stage—before the contact establishment—when the nodal temperature decreases due to the heat exchange with air, the full contact stage when the temperature increases as a result of the friction energy dissipation, and the third stage when the block leaves the contact interface and the temperature decreases again due to heat exchange with air. It should be noticed that, for the simulation with initial block temperature $T_{B,0} = 20^\circ\text{C}$, the

TABLE 3: Loading and boundary conditions in the simulation of a rubber block moving on a tire-rotation-like displacement path.

accelerating				braking			
$\mathbf{v}_R = 300 \text{ mm/s}$				$\mathbf{v}_R = 300 \text{ mm/s}$			
$\omega_B = 1.064 \text{ rad/s}$				$\omega_B = 0.98 \text{ rad/s}$			
Sim	$T_{B,0} [^\circ\text{C}]$	$p_N [N/mm^2]$	$\mathbf{v}_T [mm/s]$	Sim	$T_{B,0} [^\circ\text{C}]$	$p_N [N/mm^2]$	$\mathbf{v}_T [mm/s]$
1	20	0.506	87.438	4	20	0.487	78.197
2	70	0.502	81.038	5	70	0.492	78.748
3	100	0.500	81.042	6	100	0.491	78.750

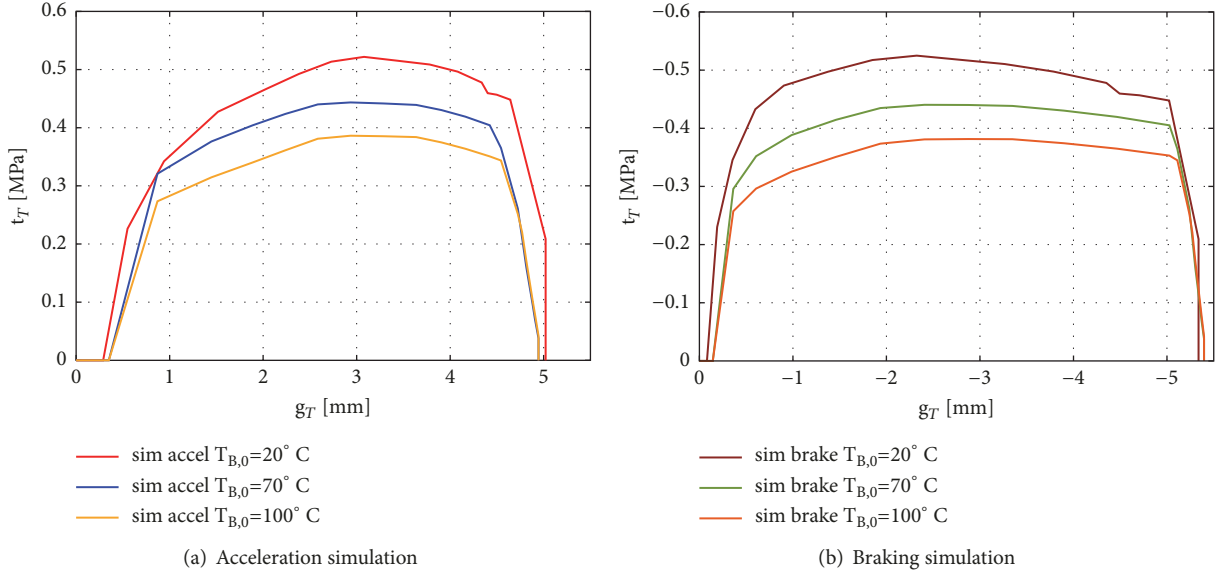


FIGURE 13: Tangential stresses versus slip in the acceleration and braking simulation.

temperature is not decreasing in stage one but stays constant due to the same magnitude of the air temperature $T_{A,0} = 20^\circ\text{C}$. The temperature increase within the simulation with $T_{B,0} = 20^\circ\text{C}$ is more pronounced than for simulations with $T_{B,0} = 70^\circ\text{C}$ and $T_{B,0} = 100^\circ\text{C}$ due to higher values of the friction coefficient μ and, therefore, higher magnitude of the dissipated friction energy \mathcal{D}_s . The same observations are valid for the results of the braking simulation presented in Figure 12(b). In this example, larger temperature amplitudes are obtained within the braking simulation than within the accelerating simulation i.a. due to a slightly larger magnitude of relative braking in comparison to relative acceleration.

In Figure 13, the tangential stresses t_T are plotted versus the tangential slip g_T . Thereby, a clear tendency characterized by achieving higher t_T at lower initial rubber block temperatures $T_{B,0}$ is visible, which is conform with the magnitudes of the friction coefficient obtained in the experiments for the contact pressure and sliding velocity ranges under consideration. Representative values for p_N and \mathbf{v}_T , which are obtained in the simulation during sliding at $g_T = \pm 3 \text{ mm}$, are shown in Table 3. Furthermore, within a single simulation at certain initial rubber block temperature $T_{B,0}$, a variation of tangential stress magnitudes in the full contact stage can be observed. This effect is achieved due to the

TABLE 4: Residual force in subsequent equilibrium iterations at two selected time increments t_1 and t_2 .

iteration	t_1	t_2
	$F_{res} [N]$	$F_{res} [N]$
1	$1.406 \cdot 10^{-3}$	$-1.545 \cdot 10^{-3}$
2	$9.356 \cdot 10^{-6}$	$4.492 \cdot 10^{-6}$

dependency of the tangential stress formulation on the local nodal pressure and temperature, which magnitudes change during the simulation.

Within this example, the rate of convergence of the formulation is examined. In almost all time increments the Newton method is able to find the solution within 1-3 iterations. Thereby, a quadratic rate of convergence is obtained, which is confirmed by the magnitudes of the residual force F_{res} in subsequent equilibrium iterations at two selected time increments t_1 and t_2 ; see Table 4. Thereby, the considered time increments refer to the time, when the rubber block is sliding on the road surface.

The presented results confirm that the application of the newly developed friction law within a thermo-mechanically

TABLE 5: Representative values of tangential stresses obtained in the FE tire simulation with corresponding p_N , v_T , and T values.

node	T [°C]	p_N [N/mm ²]	v_T [mm/s]	t_T [N/mm ²]
1	20	0.371	147.887	-0.355
1	70	0.384	181.090	-0.362
2	20	0.455	130.700	-0.396
2	70	0.467	179.130	-0.402
3	20	0.448	161.790	-0.426
3	70	0.448	514.825	-0.423

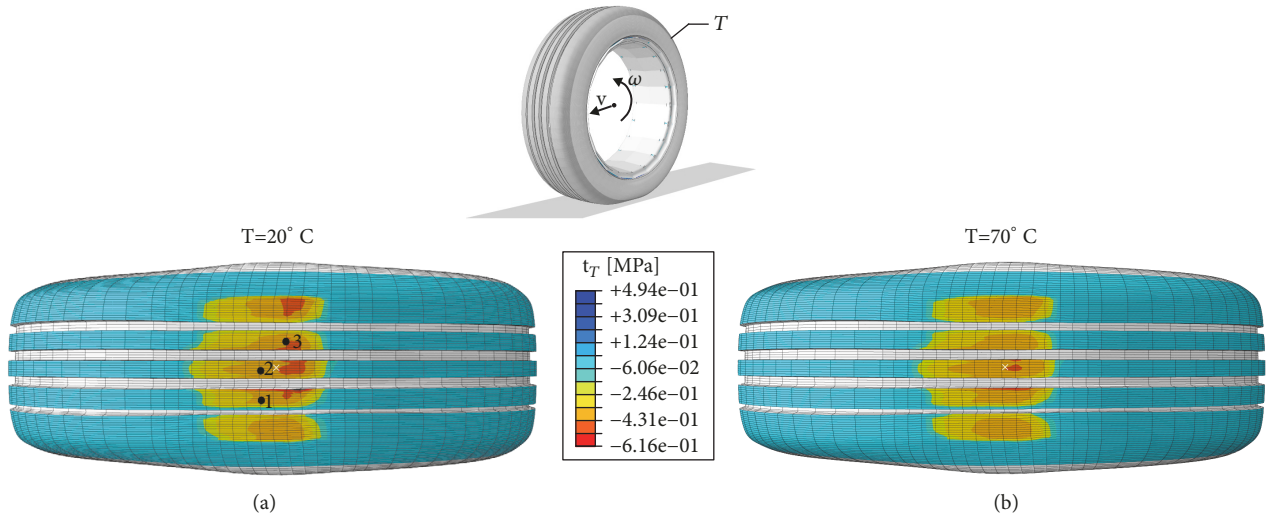


FIGURE 14: Tangential stress distribution in the contact interface of a rolling tire.

coupled FE simulation enables to properly capture the contact phenomena related to temperature and friction.

5.3. Tire Simulation. In this example, two isothermal FE simulations of tires in the steady state rolling condition are performed. In the first simulation, the temperature of all tire components is set to $T = 20^\circ\text{C}$, whereas in the second simulation to $T = 70^\circ\text{C}$. The tire is subjected to inner pressure $p = 0.26 \text{ MPa}$ and a vertical load $F_V = 5250 \text{ N}$. In both simulations, the translational velocity is equal to $v = 108 \text{ km/h}$ and the angular velocity to $\omega = 100 \text{ rad/s}$, which corresponds to a braking state; see Figure 14.

In the applied tire model, the rubber parts are discretized by 8-node hybrid solid elements, in which pressure stress is an additional independently interpolated solution variable, that is coupled to the displacement solution. Such element formulation is suited for nearly incompressible materials. The tire reinforcement is modelled by means of rebar layers embedded in the solid elements and the road is defined as a rigid body.

The FE steady state rolling analysis applied in the framework of this contribution is accomplished by means of the arbitrary Lagrangian-Eulerian approach; see [27–29]. Thus, tire rotation is regarded as a rigid body rotation and described in the Eulerian frame whereas the material deformation is described in the Lagrangian frame. The rotation is considered as a material flow through a standing FE mesh, where the

flow occurs at surface streamlines. The application of the arbitrary Lagrangian-Eulerian approach permits an adaptive discretization of the tire model, where a fine mesh is required solely in the tire-road contact zone. Thus, efficient FE simulations characterized by a low computational cost but a high accuracy can be performed.

The application of the developed friction law within a steady state transport analysis, which is stationary and thus time independent, requires the consideration of a different dependency between the sliding velocity $\|\mathbf{v}_T\|$ and the tangential slip $\mathbf{g}_{T,n+1}$ than in a transient analysis. Since this dependency is given as $\|\mathbf{v}_T\| = \|\Delta\mathbf{g}_T\|$, in equation (25), which is utilized for the specification of the algorithmic tangent, the term $1/\Delta t$ vanishes.

The results of the FE tire simulations accomplished in this study are visualized in Figure 14. Especially, the distributions of tangential stresses obtained in the FE analyses with prescribed tire temperatures $T = 20^\circ\text{C}$ and $T = 70^\circ\text{C}$ are shown. Thereby, the stress component in the driving direction of the tire is considered. In Figure 14, the tangential stresses t_T vary with respect to the local temperature, contact pressure and sliding velocity. In Table 5, representative values of t_T and the corresponding influencing factors are given for selected nodes in the tire contact area, see Figure 14. The tangential stresses on the right-hand side of the contact patch are larger in the tire simulation with tire temperature $T = 20^\circ\text{C}$ than with tire temperature $T = 70^\circ\text{C}$.

This example confirms, that the developed metamodel based constitutive equation for friction is applicable within the arbitrary Lagrangian-Eulerian approach and can be utilized in the simulation of steady state rolling tires.

6. Conclusions

In this contribution, a new friction model enabling to capture the thermo-mechanical tribological properties of elastomeric structures is proposed. The developed macroscopic equation for friction accounts for the dependency of the friction coefficient on the local contact pressure, sliding velocity and temperature in the contact interface. Since a metamodel is integrated into the friction formulation, an extraordinary high fitting quality to the experimental results is achieved. Furthermore, a consistent formulation of the law enabling its implementation within the framework of the finite element method is provided. Various applications of the proposed constitutive equation for friction to FE simulations indicate its good performance in transient isotherm and thermo-mechanically coupled analyses as well as in isotherm steady state transport analyses.

Data Availability

The data used to support the findings of this study are included within the article.

Conflicts of Interest

The authors declare that there are no conflicts of interest regarding the publication of this paper.

Acknowledgments

The authors would like to gratefully acknowledge the financial support of the Deutsche Forschungsgemeinschaft (DFG) under grant no. KA 1163/30 within the DFG research unit FOR 2089.

References

- [1] A. Serafinska, N. Hassoun, and M. Kaliske, "Numerical optimization of wear performance - Utilizing a metamodel based friction law," *Computers & Structures*, vol. 165, pp. 10–23, 2016.
- [2] G. Heinrich and M. Klüppel, "Rubber friction, tread deformation and tire traction," *Wear*, vol. 265, no. 7-8, pp. 1052–1060, 2008.
- [3] A. Le Gal and M. Klüppel, "Investigation and modelling of rubber stationary friction on rough surfaces," *Journal of Physics: Condensed Matter*, vol. 20, no. 1, 2008.
- [4] B. N. J. Persson, "Contact mechanics for randomly rough surfaces," *Surface Science Reports*, vol. 61, no. 4, pp. 201–227, 2006.
- [5] P. Wriggers and J. Reinelt, "Multi-scale approach for frictional contact of elastomers on rough rigid surfaces," *Computer Methods in Applied Mechanics and Engineering*, vol. 198, no. 21-26, pp. 1996–2008, 2009.
- [6] K. Falk, R. Lang, and M. Kaliske, "Multiscale simulation to determine rubber friction on asphalt surfaces," *Tire Science and Technology*, vol. 44, no. 4, pp. 226–247, 2016.
- [7] F. Hartung, R. Kienle, T. Götz et al., "Numerical determination of hysteresis friction on different length scales and comparison to experiments," *Tribology International*, vol. 127, pp. 165–176, 2018.
- [8] T. Huemer, W. N. Liu, J. Eberhardsteiner, and H. A. Mang, "A 3D finite element formulation describing the frictional behavior of rubber on ice and concrete surfaces," *Engineering Computations*, vol. 18, no. 3-4, pp. 417–436, 2001.
- [9] A. R. Savkoor, "Some aspects of friction and wear of tyres arising from deformations, slip and stresses at the ground contact," *Wear*, vol. 9, no. 1, pp. 66–78, 1966.
- [10] R. van der Steen, *Enhanced friction modeling for steady-state rolling tires [Ph.D. thesis]*, Technische Universiteit Eindhoven, 2010.
- [11] S. Haykin, *Neural Networks: a Comprehensive Foundation*, Prentice-Hall, 1999.
- [12] H. Adeli, "Neural networks in civil engineering: 1989–2000," *Computer-Aided Civil and Infrastructure Engineering*, vol. 16, no. 2, pp. 126–142, 2001.
- [13] C. Zopf and M. Kaliske, "Numerical characterisation of uncured elastomers by a neural network based approach," *Computers & Structures*, vol. 182, pp. 504–525, 2017.
- [14] S. Freitag, *Modellfreie numerische Prognosemethoden zur Tragwerksanalyse [Dissertation, thesis]*, Technische Universität Dresden, 2010.
- [15] A. Chamekh, H. Bel Hadj Salah, and R. Hambli, "Inverse technique identification of material parameters using finite element and neural network computation," *The International Journal of Advanced Manufacturing Technology*, vol. 44, no. 1-2, pp. 173–179, 2009.
- [16] J. L. Rogers, "Simulating structural analysis with neural network," *Journal of Computing in Civil Engineering*, vol. 8, no. 2, pp. 252–265, 1994.
- [17] W. Graf, J.-U. Sickert, S. Pannier, and M. Kaliske, "Robust design with uncertain data and response surface approximation," in *Proceedings of the 4th International Workshop on Reliable Engineering Computing (REC 2010)*, M. Beer, R. L. Muhanna, and R. L. Mullen, Eds., pp. 554–573, Singapore, 2010.
- [18] W. Graf, J. Sickert, S. Freitag, S. Pannier, and M. Kaliske, "Neural network approaches in structural analysis considering imprecision and variability," in *Soft Computing Methods for Civil and Structural Engineering*, pp. 59–85, Saxe-Coburg Publications, Stirlingshire, UK, 2011.
- [19] C. M. Bishop, *Neural Networks for Pattern Recognition*, Oxford University Press, New York, USA, 1995.
- [20] P. Wriggers, *Computational Contact Mechanics*, Wiley, Chichester, 2002.
- [21] R. S. Marlow, "A general first-invariant hyperelastic constitutive model," in *Constitutive Models for Rubber III*, J. Busfield and A. Muhr, Eds., pp. 157–160, Balkema Publications, Lisse, 2003.
- [22] O. H. Yeoh, "Some forms of the strain energy function for rubber," *Rubber Chemistry and Technology*, vol. 66, no. 5, pp. 754–771, 1993.
- [23] E. M. Arruda and M. C. Boyce, "A three-dimensional constitutive model for the large stretch behavior of rubber elastic materials," *Journal of the Mechanics and Physics of Solids*, vol. 41, no. 2, pp. 389–412, 1993.

- [24] J. C. Simo, "On a fully three-dimensional finite-strain viscoelastic damage model: Formulation and computational aspects," *Computer Methods in Applied Mechanics and Engineering*, vol. 60, no. 2, pp. 153–173, 1987.
- [25] S. Reese and S. Govindjee, "A theory of finite viscoelasticity and numerical aspects," *International Journal of Solids and Structures*, vol. 35, no. 26-27, pp. 3455–3482, 1998.
- [26] G. A. Holzapfel, "On large strain viscoelasticity: Continuum formulation and finite element applications to elastomeric structures," *International Journal for Numerical Methods in Engineering*, vol. 39, no. 22, pp. 3903–3926, 1996.
- [27] T. J. Hughes, W. K. Liu, and T. Zimmermann, "Lagrangian-Eulerian finite element formulation for incompressible viscous flows," *Computer Methods in Applied Mechanics and Engineering*, vol. 29, no. 3, pp. 329–349, 1981.
- [28] M. Kaliske, D. Zheng, M. Andre, and C. Bertram, "Efficient steady-state simulations up to high speed with dissipative tire characteristics," *Vehicle Systems Dynamics Journal Supplement*, vol. 40, pp. 175–194, 2003.
- [29] U. Nackenhorst, "The ALE-formulation of bodies in rolling contact: Theoretical foundations and finite element approach," *Computer Methods in Applied Mechanics and Engineering*, vol. 193, no. 39-41, pp. 4299–4322, 2004.

